THE ASTROPHYSICAL JOURNAL, 950:74 (11pp), 2023 June 10 https://doi.org/10.3847/1538-4357/acc656

The Large Magellanic Cloud Supernova Remnant MCSNR J0550-6823

Frederick D. Seward[1] and Sean D. Points[2]
[1] Smithsonian Astrophysical Observatory, 60 Garden St., Cambridge, MA 01238, USA
[2] Cerro Tololo Inter-American Observatory/NOIRLab, Casilla 603, La Serena, Chile
Received 2022 December 4; revised 2023 March 17; accepted 2023 March 20; published 2023 June 12

Abstract

We describe radio, optical, and X-ray observations of this rather faint, old Large Magellanic Cloud (LMC) supernova remnant. The [O III] emission forms a distinct shell, the remnant of the outer shock, which encloses the radio and X-ray emission and gives an estimate of age and explosion energy. Because of a collision with an LMC Hα filament, radio and X-ray emission are concentrated in the northern half of the remnant. The X-ray spectrum is well fit assuming the plasma is isothermal and in collisional equilibrium. The best-fit temperature is such that almost all energy is in lines from O, Ne, Mg, and Fe. The known distance, low extinction, and low interstellarmedium metallicity allow derivation of masses of several elements produced by the star and in the explosion. The masses of O, Ne, and Fe point to a Type II supernova from the explosion of a 20–25 $M_\odot$ star. The mass of Mg, however, is higher than that of almost all predictions, but some of this apparent excess might be due to a higher-temperature region in the X-ray-emitting material. Point-like background sources are examined to search for a neutron star, and one possible candidate is found just inside the shell of the remnant.

Unified Astronomy Thesaurus concepts: X-ray astronomy (1810); Large Magellanic Cloud (903); Type II supernovae (1731); Supernova remnants (1667)

1. Introduction

MCSNR 0550-6823 (hereafter SNR 0550) is located at the eastern edge of the Large Magellanic Cloud (LMC). It was observed by Chandra in 2003 October and the resulting image and spectrum were placed in the Chandra online SNR catalog.[3] The outer shell has an elliptical shape with dimension $4\overset{'}{.}9 \times 6\overset{'}{.}1$, which at the LMC distance of 50 pc is 71×88 pc, making this is one of the largest remnants in the Magellanic Clouds (MCs) known to be a source of X-rays. This paper, using archival reprocessed data, presents a description of the X-ray morphology and spectrum, calculates the mass of O, Ne, Mg, and Fe in the X-ray-emitting hot gas, and compares results with predictions of stellar explosions. We will show that the evidence points to a Type II supernova (SN) explosion of a $\geqslant$20 $M_\odot$ star.

In addition to the interest in this particular remnant, this information is useful in comparison with other well-studied MC remnants (Maggi et al. 2016; Bozzetto et al. 2022). The $\approx$80 MC remnants, because of low absorption and known distance, form a unique group that bridges the gap between studies of the galactic remnants and studies of those in more distant galaxies, e.g., M33 (Long et al. 2010) and M31 (Sasaki et al. 2012). The MC sample is close enough to distinguish between the remains of Type I and Type II SN explosions and to sometimes detect associated neutron stars (NSs). Although NSs associated with older remnants such as SNR 0550 are expected to be faint (Haberl 2007), we search for a possible brighter example of a central compact object by looking at counterparts and spectra of surrounding serendipitous sources.

[3] http://hea-www.cfa.harvard.edu/ChandraSNR

2. Optical Observations

2.1. Magellanic Cloud Emission Line Survey Images

For comparison with optical wavelengths, we used images from the Magellanic Cloud Emission Line Survey (MCELS; Smith & MCELS Team 1998). The reduction details of the MCELS images are discussed in Seward et al. (2021).

The energy radiated by the filaments within the remnant, as seen in Figure 1, was calculated by overlaying a circle with a radius of 180″ to include all emission from the shell and integrating the enclosed signal with bright stars excluded. This region was selected to include emission from the supernova remnant (SNR) that has a [S II]:Hα ratio of $\geqslant$0.4, which is an optical diagnostic used to separate shock-ionized gas from photoionized material (Dopita 1982) and also includes the region of diffuse X-ray emission. A nearby region southeast of the remnant was used to calculate the background. This resulted in an observed Hα flux from the SNR of 6.27×10^{-12} erg s^{-1} cm^{-2}.

The extinction was first obtained using the work of Zaritsky et al. (2004) to average the extinction of 106 stars over the area of the remnant, resulting in a mean extinction of $\langle A_v \rangle = 0.50 \pm 0.41$ mag. Given the large uncertainty associated with this extinction value, we decided instead to use the same absorbing column as used in the X-ray analysis, $N_{\rm H} = 1.6 \times 10^{21}$ cm^{-2} (see Section 3.6) with column density converted to A_V using the relation given by Güver & Özel (2009): $N_{\rm H}({\rm cm}^{-2}) = 2.21 \pm 0.09 \times 10^{21}$ A_V(mag), resulting in an A_V of 0.72 ± 0.03 mag. $A({\rm H}\alpha) \approx A([{\rm S\,II}]) = 0.81$ $A_v = 0.81 \times 0.72 = 0.59$ mag was applied to get the corrected [S II] and Hα fluxes. At [O III], the extinction $A([{\rm O\,III}])$ $\sim$ 1.1 $A_v = 0.80$ mag was applied to get the corrected [O III] flux. Extinction-corrected fluxes and luminosities are listed in Table 1. Uncertainties were 8% in background subtraction, 5%–10% in the calibrations, and 3% in extinction, $\approx$15% total.

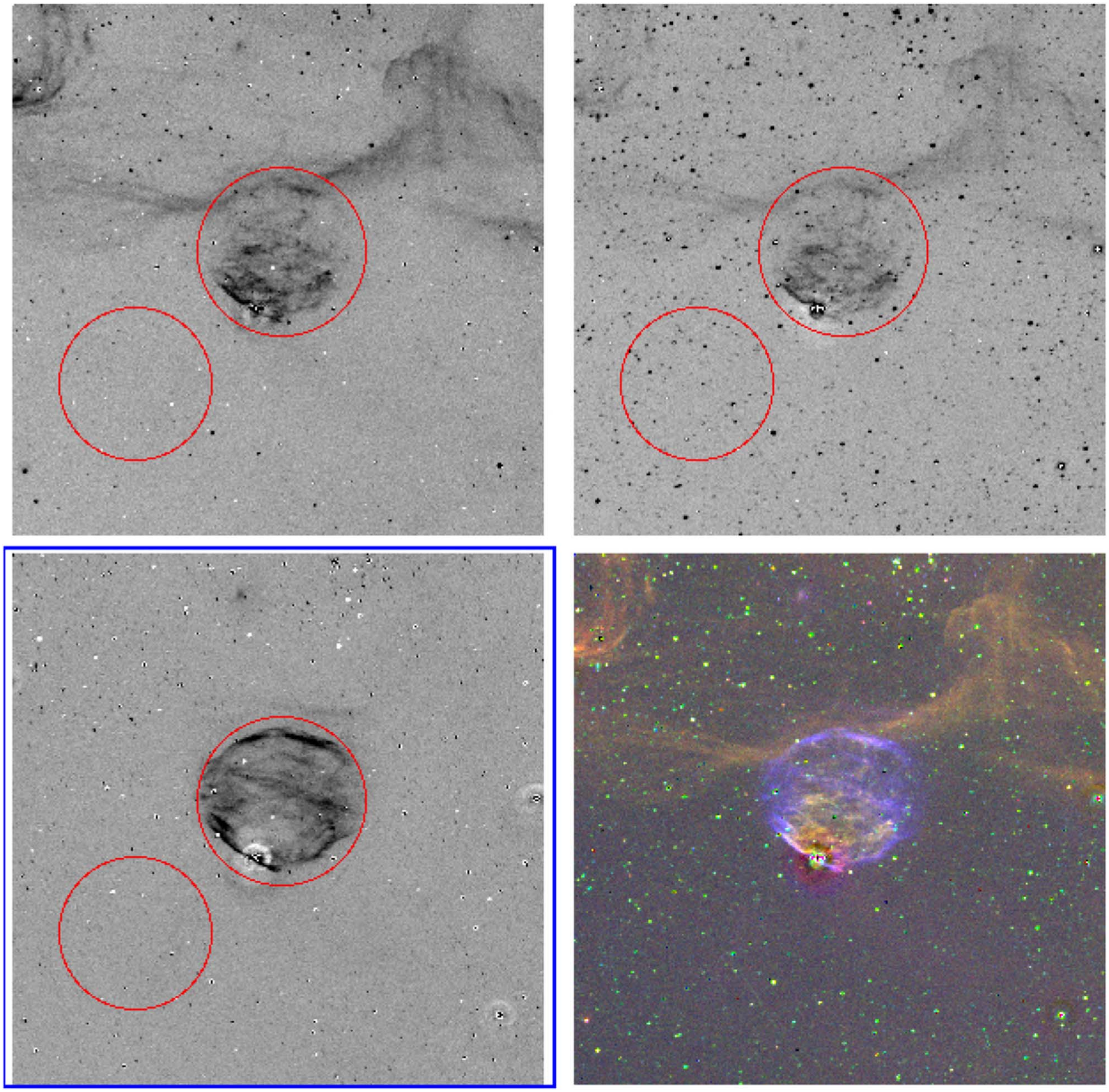

Figure 1. Appearance of the remnant in three spectral lines: Each frame is 27′ square. North is up, east is left; upper-left image, Hα; upper right, [S II]; lower left, [O III]; lower right, color overlay with R, G, and B showing H, S, and O. The red circles show areas used to determine flux and associated backgrounds.

2.2. Temperature and Density

The Hα surface brightness (SB) of a 10^4 K ionized gas region can be expressed as $\mathrm{SB} = 1.9 \times 10^{-18} n_e^2 L_{\mathrm{pc}}$ erg cm^{-2} s^{-1} arcsec^{-2}, where n_e is the rms electron density and L_{pc} is the emitting path length in parsecs along the line of sight (Rozas et al. 2006). If we assume a simple shell geometry and uniform density of the shell, the peak surface brightness occurs at the longest line of sight through the shell, L. The longest line of sight is calculated from the shell thickness, ΔR, and radius, R, to be $L = 2[\Delta R(2R - \Delta R)]^{1/2}$.

The Hα filament with the highest surface brightness is located along the southeastern rim of the SNR shell and, measured from the image at this point, $\mathrm{SB} = \sim 6.86 \times 10^{-14}$ erg s^{-1} cm^{-2} arcsec^{-2}, corrected for reddening. We find that the average thickness of the shell, ΔR, is 9″.5 (2.37 pc) and the shell radius, R, to be ∼150″ (37.5 pc). Thus, the path length through the shell, L, is 26 pc and the electron density, n_e, is 37 cm^{-3}.

Table 1
Luminosity and Density of Optical Filaments

Ion	λ (Å)	Unabs. Flux (erg cm^{-2} s^{-1})	Luminosity (erg s^{-1})	Density (cm^{-3})
H I	6563	1.08×10^{-11}	$(3.2 \pm 0.5) \times 10^{36}$	37
37O III	5007	1.55×10^{-11}	$(4.6 \pm 0.7) \times 10^{36}$	
S II	6724	7.00×10^{-12}	$(2.1 \pm 0.3) \times 10^{36}$	

2.3. The Outer Shock and a Collision

The [O III] appearance is almost circular and unusually symmetrical for an older remnant. There is strong limb brightening around half the circumference and the shape is

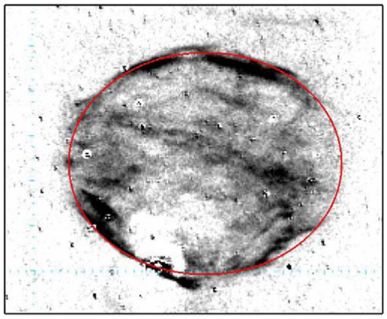

Figure 2. MCELS [O III] emission and ellipse used to represent the dense shell. A bright star at the southeast edge has been subtracted.

close to an ellipse, with semimajor and semiminor axes 182″ and 148″ (44.0 × 35.8 pc), as shown in Figure 2. We take this as the recent appearance of a dense shell formed when the outer shock started to cool and radiate strongly. The Hα and [S II] images have lesser limb brightening in the north but relatively more emission from the southern area, including arc-like structures inside of and parallel to the southern edge of the dense shell.

The Hα and [S II] images show this dense shell interacting with a long interstellar filament north of the remnant. Material has been pushed from this filament ahead of the expanding shell; this is not an overlap due to projection but a real interaction. Since there is very little of this Hα-emitting material visible in the line of sight passing just inside the remnant shell, this is not a sheet of material but a narrow filament; at least the line-of-sight dimension of the apparent filament is less than the radius of the SNR shell. The [O III] shell is brighter over the colliding region but there is little distortion of the shell. The Hα and [S II] also show a brightening and no distortion at the collision site. Apparently the dense-shell expansion is not much impeded. The displaced filament material must have been been moved by a forward collision shock, although this shock front is not apparent in the images. The reverse collision shock has traveled faster in the high-temperature plasma inside the remnant and has further heated and compressed material in the northern interior. Radio emission from this location implies a magnetic field, probably compressed by the collision shock, which may also have accelerated the radio electrons.

3. X-Ray and Radio Morphology

3.1. Chandra X-Ray Observation

SNR 0550 was observed on 2003 October 2 with the Chandra ACIS-S array, and 67 ks of low-background data were obtained (Obsid 3850). Of the more than 50 MC remnants observed by Chandra, ranked by X-ray brightness, SNR 0550 is among the lower third. Although not one of the brighter remnants, this observation was early in the Chandra mission and the ACIS detector sensitivity (falling due to a buildup of contamination on the detector window) was high enough to collect counts adequate for a reasonable analysis.

Because the source is large and faint, the number of background counts subtracted is relatively large. In this case, 11,090 counts were collected from the area inside the remnant, of which 3170 were background, and 7920 were diffuse emission from SNR 0550. Figure 3 shows this diffuse emission compared with the position of the cooling outer shock. The brightest interior X-rays form a patchy structure filling most, but not all, of the central area. The faintest diffuse emission does not fill the interior in the far-northern and mid-to-far-southern parts of the remnant. There is no indication of a central X-ray-emitting NS.

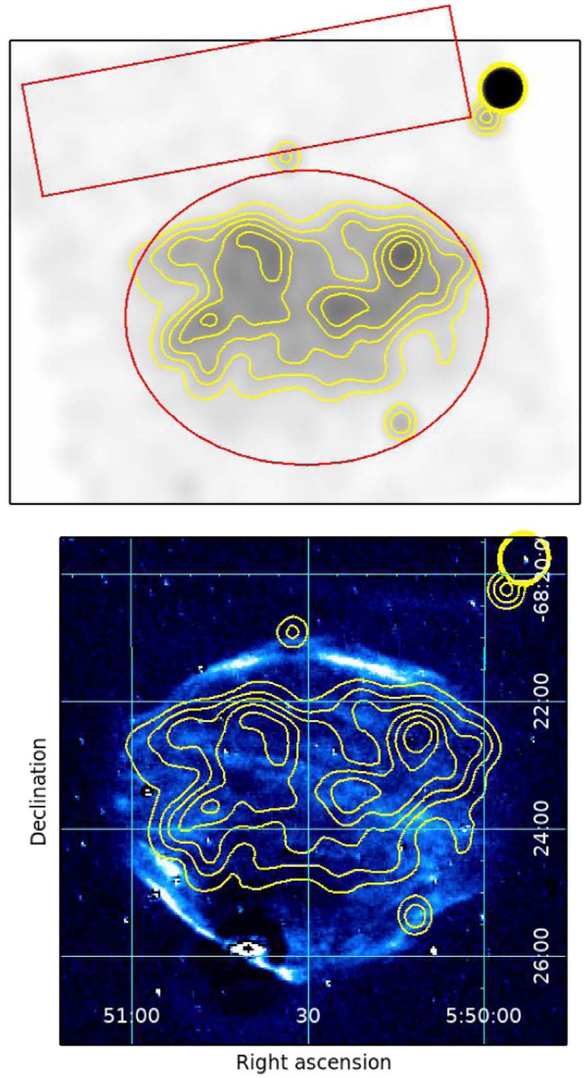

Figure 3. Top: X-ray image in the energy range 0.4–1.5 keV with 10″ Gaussian smoothing. The point radio and X-ray source touching the northern remnant boundary is the background active galactic nucleus described in Section 7. Three other point sources are visible, one just inside the southern boundary. The red ellipse marks the outer (dense) shell and the red rectangle shows the region used for X-ray background subtraction. Bottom: contours of 0.4–1.5 keV X-ray surface brightness are overlaid on the MCELS map of [O III] emission, which marks the outer shell. The [O III] stretch is linear and the X-ray contours are evenly spaced at intervals of 0.50×10^{-8} photons cm^{-2} s^{-1} arcsec^{-2}, with the largest (minimum value) contour having a value 1.0×10^{-8}.

3.2. Radio Observation

The radio emission was mapped at 3 and 6 cm in 2001–2003 by Dickel et al. (2005), and in 1997 by Bozzetto et al. (2012). Bozzetto et al. (2012) measure a broken power-law radio spectrum with a polarization of 50% and remark that both are unusual for an LMC remnant. In 2020 the remnant was included in a 33 cm LMC survey by the Australian Square Kilometer Array Pathfinder telescope (Pennock et al. 2021),

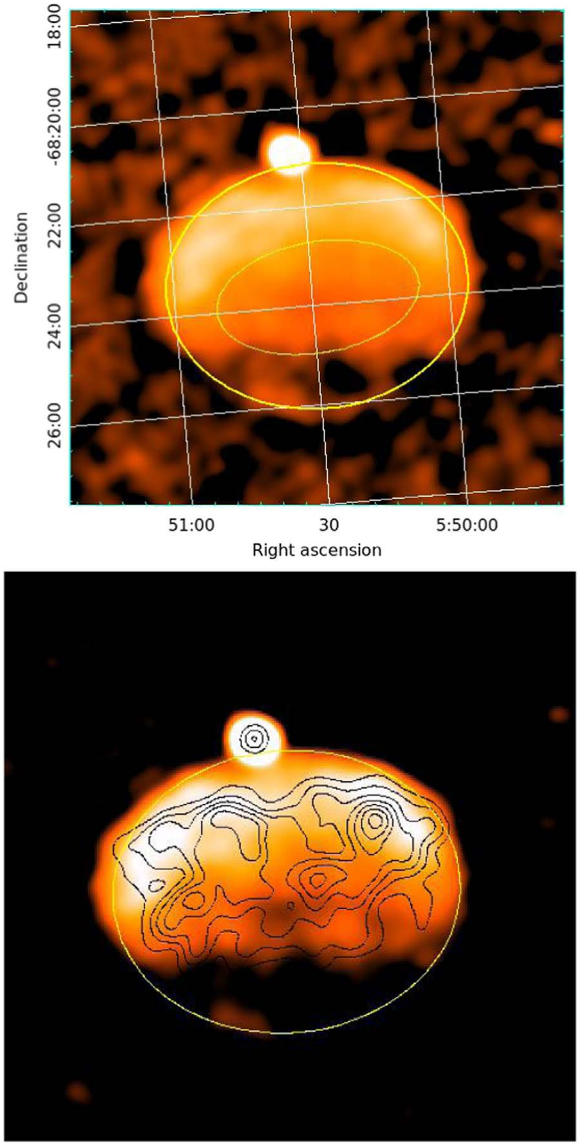

Figure 4. 33 cm radio image and comparison with X-rays. The large yellow ellipse marks the position of the outer edge of the [O III] shell. Top: the radio image with a square-root stretch adjusted to show faint emission. The size of the radio beam was 12″ × 14″. The brightest emission is from the broad northern arc interior to the [O III] shell and there is clearly weaker emission extending through the center to the southern edge of the remnant. The interior yellow ellipse defines a "central" region used for spectral analysis. The shape of this smaller ellipse was set to fit the inside edge of the bright radio arc. Bottom: radio image and X-ray surface-brightness contours are overlaid. X-ray contours are the same as those in Figure 3 and the square-root stretch of the radio image is adjusted to show structure in the bright northern arc. The faint green ellipse closely follows the faintest X-ray contour and was used to extract data concerning the total X-ray emission.

and Figure 4 shows the 33 cm image overlaid with the X-ray surface-brightness contours shown in Figure 3.

The radio emission is also almost all from the broad northern arc which, like the X-ray arc, is bright and irregular. The brightest X-ray and radio regions do not correspond exactly, but the central azimuthal minimum in the radio arc does overlay a corresponding X-ray minimum.

Figures 3 and 4 show that the material strongly emitting both radio and X-rays is well inside the [O III] shell, which defines the outer shock. Radio emission does extend slightly outside of the ellipse marking the [O III] shell in the east, where the [O III] emission itself is indistinct. In the southern half of the remnant, both radio and X-ray emission are faint, but there is a somewhat brighter radio wisp following along the southern border with surface brightness ∼10% that of the northern arc. A corresponding X-ray feature is not detected. The brightest radio spots are slightly farther from the center than nearby X-ray bright spots.

3.3. Morphology and Structure

All diffuse X-rays come from the interior of the shell defined by the [O III] emission. Figures 3 and 4 show the smoothed fluxed image. The maximum X-ray surface brightness is from a spot in the northwest with extent ≈1′. There are other emission maxima in the northeast, southeast, and one close to the center of the [O III] ellipse, which traces the cooling outer shock. The brightness of the northwest peak is ∼3× that of the diffuse central area and the brightness of the other three maxima is ∼2× that of the center. Since the emitting material is clumpy, in the derivation of electron density a filling factor, *f*, allows for the nonuniform distribution.

The apparent elemental distribution varies. Figure 5 shows images made using only events from energies within the visual peaks in the spectrum due to the three strong lines from O, Ne, and Mg. Adaptive smoothing (CIAO task *asmooth*) was used because there were not many photons in these narrow energy bands. The first image in Figure 5, however, was made using the entire spectrum for comparison to the Gaussian-smoothed image in Figure 3. The overall structure is the same, but unevenness in small-scale structure is suppressed in the adaptive smoothing. The smoothed images of emission from the three elements are all different. The O emission shows maxima in the same four places as the total emission. The Ne image shows one broad peak, which coincides with the northwest maximum. The Mg image has only one broad maximum of emission, located close to the remnant center.

If the plasma temperature and density were uniform, this variation could be attributed to varying concentration of the elements. However, at this temperature ($kT = 0.282 \pm 0.007$ in Table 2), the emission measure of O is falling, that of Ne is rising slowly with increasing temperature, and that of Mg is rising rapidly. An increase of ≈10% in kT in a collisional ionization equilibrium plasma would result in emission changes of ≈−16% for O VII+O VIII, ≈+8% for Ne IX, and ≈+45% for Mg XI.[4] To search for a temperature difference, we looked at small regions that included events within a radius of 40″ around the northwest maximum (O max.) and around the central maximum (Mg max.). These spectra appeared almost identical but with large uncertainties, so there was no useful result.

3.4. Two Spectral Regions

Visual inspection of spectra from different areas shows almost no change in spectral form, but the uncertainties become large for small samples. We divided the remnant into two parts: an arc coinciding with that of the radio emission, and an inner "central" region, each with ≈3700 counts. Noting the shell-like form of the radio emission, the southern edge of the bright radio arc was used to define a "central" region of the remnant, shown in Figure 4 as the small ellipse (semi-axes 67″ × 123″).

[4] atomdb.org/Webguide

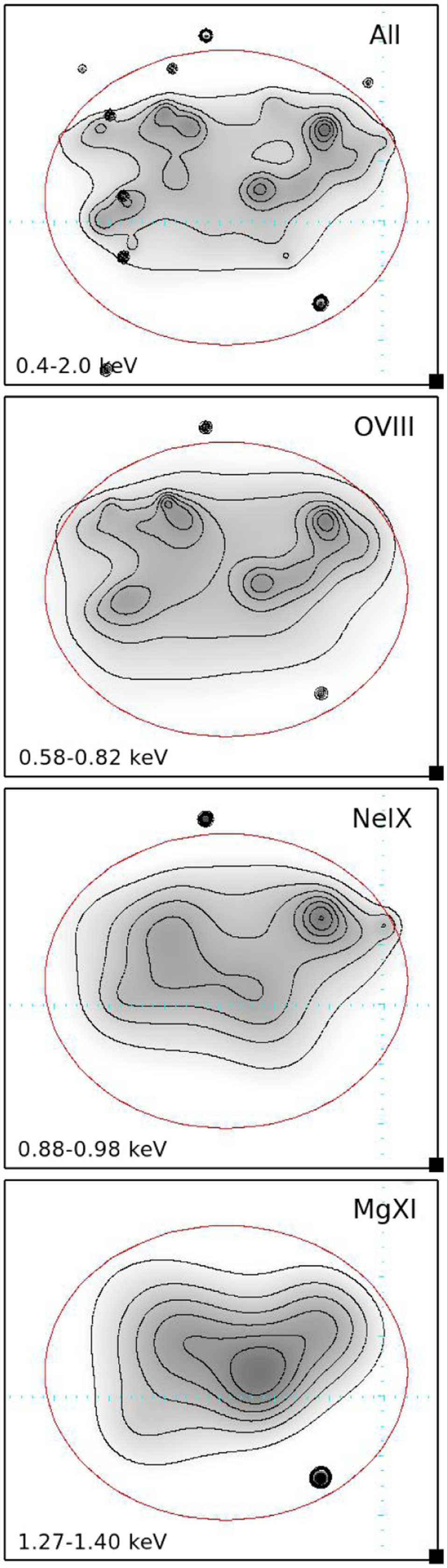

Figure 5. Adaptive smoothing of a fluxed image made with events of all energies and of images with only events from narrow energy bands centered on emission lines from single ions: O VIII, Ne IX, and Mg XI. The stretch is square root and contours are evenly spaced with brightness increments for the respective figures of 0.25, 0.10. 0.025, and 0.01 × 10^{-8} photons cm^{-2} s^{-1} $arcsec^{-2}$.

One can imagine the bright arc continuing south of the central part to form a ring, all within the O III shell and with southern half too cool for X-ray emission.

Thus, the actual X-ray-emitting region was split into a half-shell and a central region. Abundances in these two regions were determined after fixing the Si abundance to improve the measure for other elements allowed to vary. Table 2 lists the spectral parameters, and the temperature of the central region is indeed 0.030 ± 0.013 keV higher than that of the shell. Thus, the abundance of Mg in the central concentration derived using the isothermal plasma assumption and data from the entire remnant appears higher than it actually is. It could be ≈20% higher. There are implications for the ejecta masses to be determined in the following sections.

3.5. Spectrum

Events for spectrum and background were extracted from regions shown in Figures 3 and 4. Diffuse emission from the remnant was taken from an area including all bright emission but smaller than that inside the O[III] shell.

The background varies throughout the ACIS chip field, mostly at low and high energies. We use data in the 0.4–2.0 interval, avoiding large 0.3 and small 2.1 keV maxima in the background. There is a small 0.5 keV background feature, which is negligible; but at 1.7–1.8 keV there are considerably more counts in the background than from the remnant, rendering detection of the Si line at 1.85 keV doubtful, so the energy range for some spectra was reduced to 0.4–1.6 keV. The background used was taken from a large region north of, and well separated from, the remnant (Figure 3).

After background subtraction and grouping over two energy bins, the spectrum was fit using Chandra CIAO software and SHERPA v4.14.0 (Freeman et al. 2001). To determine sensitivity to background, we repeated the spectral fit using a somewhat higher background taken from an elliptical annulus surrounding the remnant. Differences in derived model parameters were well within the uncertainties listed in Table 2.

The spectrum for the entire remnant is shown in Figure 6. Almost all the emission is in discrete lines. The strongest feature is a blend of lines from O VII at ≈0.57 keV and O VIII at 0.65 keV. There are two moderately strong lines from Fe XVII: one, at 0.72 keV, is not resolved from the O lines; the other, at 0.85 keV, is close to the stronger 0.92 keV line from Ne IX. Mg XI at 1.35 keV is a strong isolated peak and Si XIII at 1.85 keV is weak and uncertain.

This spectrum was fit assuming an isothermal plasma in collisional equilibrium (*xsvapec*) with photoelectric absorption in the intervening interstellar material (*xsphabs*). The fitting program used the *moncar* method to avoid settling into false minima, then a faster method, *levmar*, to get uncertainties. The best fit is overlaid in Figure 6, and the parameters are listed in Table 2. To fit this spectrum, LMC abundances were set at 0.3 solar for all elements except for those listed in Table 2, which were allowed to vary. Uncertainties given for each variable are 1σ and take into account possible variations of the other variables. The Si line is problematic. Although it seems definite in the spectrum, it is strong and variable in the background and the background-subtraction uncertainty is large.

A nonequilibrium ionization (NEI) model (*xsvnei*) gave good spectral fits for τ values $>5 \times 10^{10}$ cm^{-3} s. The fit, however, is not as good as that of the equilibrium fit. The minimum value

Table 2
Best-fit Spectral Parameters

Model	N_H (at cm^{-2})	kT (keV)	O	Ne	Mg Abundance (Solar)	Si	Fe	Norm (C_n) (cm^{-5})	χ^2
TE	0.06×10^{22} [a]	0.314 ± 0.008	1.09 ± 0.26	1.39 ± 0.34	3.35 ± 0.92	3.78 ± 2.01	0.26 ± 0.07	$(3.68 \pm 0.80) \times 10^{-4}$	1.38
TE	0.16×10^{22}	0.282 ± 0.007	0.67 ± 0.14	0.78 ± 0.17	2.02 ± 0.50	2.70 ± 1.33	0.18 ± 0.04	$(9.52 \pm 1.77) \times 10^{-4}$	1.34
TE	0.24×10^{22} [b]	0.254 ± 0.006	0.51 ± 0.11	0.58 ± 0.13	1.68 ± 0.42	2.65 ± 1.28	0.16 ± 0.04	$(1.88 \pm 0.34) \times 10^{-3}$	1.39
TE shell	0.16×10^{22}	0.267 ± 0.009	0.45 ± 0.10	0.59 ± 0.19	1.47 ± 0.42	0.3	0.14 ± 0.04	$(7.0 \pm 1.2) \times 10^{-4}$	1.03
TE central	0.16×10^{22}	0.297 ± 0.010	1.23 ± 0.47	1.27 ± 0.48	3.45 ± 1.38	0.3	0.27 ± 0.11	$(2.7 \pm 0.55) \times 10^{-4}$	1.45
NEI	0.16×10^{22}	0.507 ± 0.064 $\tau = 5\mathrm{e}10$	0.40 ± 0.07	0.68 ± 0.13	1.21 ± 0.24	0.91 ± 0.46	0.18 ± 0.04	$(3.28 \pm 0.74) \times 10^{-4}$	1.54

Notes.
[a] Remnant located at near side of LMC.
[b] Remnant at far side of LMC.

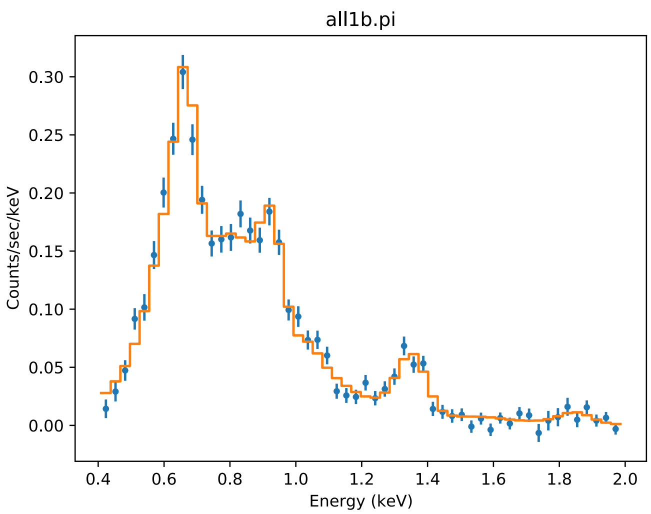

Figure 6. X-ray spectrum of MCSNR J0550-6823 in the energy range 0.4–2.0 keV. In order of energy, prominent strong lines are from O VIII, Fe XVII (which fills the space between O and Ne), Ne IX, and Mg XI. The red curve shows the best-fit isothermal/single-temperature model result.

of the ionization constant, τ, and the electron density derived from parameters of the NEI model implies a lower age limit of $5 \times 10^{10}/(0.076)(3.156 \times 10^{10}) = 21$ kyr.

3.6. X-Ray Absorbing Column

The absorbing column was taken from the H I survey of Staveley-Smith et al. (2003). The galactic column is 0.6×10^{21} atoms cm^{-2}. The LMC column at the remnant center is 2.8×10^{21} atoms cm^{-2} and ranges from 2.4 to 2.9×10^{21} atoms cm^{-2} over the face of the remnant. Taking into account the lesser O abundance of the LMC interstellar medium (ISM), the equivalent absorbing column in our energy range is about three-quarters of this (Morrison & McCammon 1983). If the remnant is at the midpoint of the LMC absorption, the equivalent column, LMC and galactic, would be 1.6×10^{21} atoms cm^{-2}. We explored a broad range of absorption values, and this is in the middle of a very shallow minimum of a χ^2 versus N_H curve. Since almost all events are from a few narrow spectral lines, good fits can be obtained from a wide range of absorbing column values by adjusting only the element abundances. For this spectrum, goodness of fit is not very sensitive to N_H. We froze the absorbing column at 0.16×10^{22} for most spectral fits, which puts the remnant at the midpoint of the LMC column. To illustrate uncertainty due to difficult to determine column thickness, much of the analysis shown is also repeated for absorptions of $0.06/0.24 \times 10^{22}$ atoms cm^{-2}, which places the remnant on the near/far side of the LMC absorbing material.

3.7. Density and Mass

If the diffuse gas were isothermal and uniform in composition, the electron density, n_e, and mass of material could be simply calculated. However, the gas composition and temperature are not strictly uniform so the resulting mass is an approximation. Inside the remnant there are no unresolved features that might be part of the diffuse structure, so the assumption of constant density is not unreasonable. Since the distance to the LMC is well known, the size of the ellipse (axes a, b) used to define the diffuse region is also well determined. The line-of-sight dimension is an assumption and we use an average of major and minor axes, $(ab)^{1/2}$. A filling factor, $f = 0.5$, was estimated by assuming the density throughout was the same as the density in a line-of-sight column including the brightest region of the remnant.

The spectral normalization constant, $C_n = 10^{-14}(4\pi D^2)^{-1} n_e n_H V f$ cm^{-5}, where D and V are the distance (in centimeters) and volume of the extraction region (in cubic centimeters). For the LMC, $4\pi D^2 = 3.00 \times 10^{47}$ cm^2, and for the extraction ellipsoid indicated in Figure 4, $V = 4.51 \times 10^{60}$ cm^3. Setting $n_e = 1.22\ n_H$ and $n_H = 1.10\ n_{\rm ion}$, the mass of diffuse material is $1.18\ m_p n_e V f$, where m_p is the proton mass in g. The internal thermal energy is $1.5\ kT\ (n_e + n_{\rm ion}) V f$. Values are listed in Table 3.

4. The Nature of MCSNR J0550-6823

4.1. The Explosion

This remnant is similar to another old LMC remnant, MCSNR J0453-6655, in the H II region N4, which we have observed previously (Seward et al. 2018). We now apply to MCSNR J0550-6823 the same analysis based on a study by Chevalier (1974), which shows the evolution of a remnant expanding into a uniform medium with magnetic field and ionized material of density n_0. The parameters of Chevalier's Model A are as follows: explosion energy $= E_0 = 0.3 \times 10^{51}$ erg and $n_0 = 1$ atom cm^{-3}. Internal and radiated energy are tracked as a function of time, and Model A shows the end

Table 3
Characteristics of Diffuse Gas

Temperature (keV)	Absorbed Flux 0.4–2.0 keV (erg cm^{-2} s^{-1})	Unabsorbed Flux 0.4–2.0 keV (erg cm^{-2} s^{-1})	L_X 0.4–2.0 keV (erg s^{-1})	Electron Density n_e (cm^{-3})	Thermal Energy (erg)	Mass ($M_\odot$)
0.314[a]	4.34×10^{-13}	5.81×10^{-13}	1.74×10^{35}	$0.077 \pm .012$	2.5×10^{50}	170
0.282	4.34×10^{-13}	9.88×10^{-13}	2.96×10^{35}	0.123 ± 0.016	3.6×10^{50}	273
0.254[b]	4.34×10^{-13}	1.57×10^{-12}	4.71×10^{35}	0.173 ± 0.022	4.5×10^{50}	384

Notes.
[a] Remnant located at near side of LMC.
[b] Remnant at far side of LMC.

of adiabatic expansion and formation of the dense radiative shell at age $t_{\rm shell} = 45$ kyr and with radius $R = 17$ pc. The internal energy, initially $0.7E_0$, starts to drop after 30 kyr, and at 45 kyr, when the thin shell has formed, is $\approx 0.5E_0$ and rapidly falling. At 100 kyr it is $\approx 0.1E_0$.

To apply to SNR 0550, we note that there is a clear [O III] shell and assume that we are observing the remnant just after radiative shell formation. The size of the [O III] shell is well known because the LMC distance is known. The shape is elliptical with semi-axes $a/2$, $b/2$, so the "radius" is taken as $0.5(ab)^{0.5} = 40$ pc and is used to scale the Chevalier model. This fixes the scale parameter as 0.425, which sets $E_0 = 1.66 \times 10^{51}$ erg, $n_0 = 0.42$ cm^{-3}, and the age $t_{\rm sh} = 94$ kyr. At this time the scaled thermal energy inside the shell is $E_{\rm th} = 0.70 \times 0.67 \times 1.66 \times 10^{51} = 0.78 \times 10^{51}$ erg (70% of E_0 less 33% radiated). The observed result is $E_{\rm th} = 1.5kT(n_e + n_{\rm H})Vf = 0.37 \times 10^{51}$ erg, about half of this. Table 4 lists our results and those from the scaled model.

The ISM density, n_0, is that of material outside the dense shell. The density derived from the X-ray observation, n_e, is that of the hot plasma inside the shell. Since the forward shock has cooled and no longer emits X-rays, they must come from material heated by the reverse and collision shock. The Chevalier model shows density varying from 0.1 to 0.9 that of n_0 from a broad region just inside the dense shell. We measure $n_e = 0.123$, which is $\approx 1/3$ the scaled $n_0 = 0.44$, in rough agreement with the scaled model. However, the density now is probably more than it would be if there were no ongoing collision shock, so comparison with the model is not exact.

The scaled model with age $\approx$94 kyr and $E_0 \approx 1.6 \times 10^{51}$ erg predicts $E_{\rm th}$ twice that observed, implying that half of the interior material has cooled below the threshold for X-ray emission. The Hα and [S II] images actually show cooler material in the southern part of the remnant where there is no X-ray emission. The implications of possible cooled ejecta are discussed in the next section.

4.2. Ejecta Element Masses

The measured abundances of O, Ne, and Mg are considerably greater than those expected in the LMC ISM. We take these excesses to be ejecta from the explosion as well as circumstellar material produced during evolution of the star. Note that the Mg concentration increases as it gets closer to the apparent center of the explosion and the Ne and O are more dispersed and concentrated at larger radii. A stratification of ejecta, perhaps?

Ejecta element masses can be estimated by subtracting the mass of the ISM component (now mixed with ejecta), which is assumed to have the LMC abundances determined by Schenck et al. (2016). Uncertainties listed in Table 5 are from combined

Table 4
MCSNR J0550-6823 Parameters from Model Comparison

	$R_{\rm sf}$ (pc)	n_e (cm^{-3})	n_0 (cm^{-3})	E_0 (erg)	$E_{\rm th}$ (erg)	$t_{\rm sf}$ (kyr)
Obs.	40	0.123	⋯	⋯	3.6×10^{50}	⋯
Model	40	⋯	0.44	1.66e51	7.8×10^{50}	94
Meas.[a]	40	0.076	⋯	⋯	2.5×10^{50}	⋯
Meas.[b]	40	0.173	⋯	⋯	4.5×10^{50}	⋯

Notes.
[a] Remnant located at near side of LMC.
[b] Remnant at far side of LMC.

LMC ISM and Sherpa-fit spectral abundances. We have also added an uncertainty of half the LMC abundance value of each element to allow for possible nonuniformity in the LMC ISM. This covers the dispersion noted in the $\sim$12 regions measured by Schenck et al. (2016). In fact, the derived masses of the O, Ne, and Mg ejecta are large enough to be rather insensitive to the values assumed for the ISM abundances. The derived Fe mass, however, is small, even smaller then our uncertainty, and is treated as an upper limit. Although the derived Si mass is large, it is also treated as an upper limit because of the large and uncertain background subtraction. Solar abundances used are from Anders & Grevesse (1989).

5. The Precursor Star

The large amount of O and the small mass of Fe leave little doubt that this remnant was produced by a Type II SN. By comparing the observed masses of O, Ne, and Mg with nucleosynthesis calculations, the mass of the precursor star can be roughly determined. Table 6 shows some comparisons taken from explosions calculated by Tsujimoto et al. (1995), Woosley & Weaver (1995), and Sukhbold et al. (2016; hereafter TNY, WW, and SEW). Numbers in the calculation identifiers are the precursor masses; to compress the table, we have omitted an "A" at the end of some of the WW identifiers. The first column of Table 6 gives the observed masses from Table 5 with 1σ uncertainties. The Si upper limit is 1σ and the Fe upper limit is 3σ.

TNY give tables of element masses from seven precursor stars with a mass range 13–70 $M_\odot$. WW lists the mass of isotopes produced in 46 explosions of progenitors with various metalicities and a mass range 11–40 $M_\odot$. These masses refer to a time 7 hr after the explosion so we have included the Ni^{56} mass with that of the decay product, Fe^{56}, in Table 6. SEW list results from a 15 and a 25 $M_\odot$ precursor.

Table 5
Mass ($M_\odot$) of Elements in Diffuse Material

Object	N_H 10^{21}	Total Mass	O	Ne	Mg	Si	Fe
Sun		100	0.960	0.175	0.066	0.071	0.127
remnant	1.6	100	0.643±00.134	0.137 ± 0.030	0.134 ± 0.033	0.192 ± 0.095	0.023 ± 0.005
LMC ISM		100	0.124 ± 0.062	0.035 ± 0.0175	0.013 ± 0.0065	0.020 ± 0.010	0.019 ± 0.0095
ejecta	1.6	(273)[a]	1.41 ± 0.36	0.28 ± 0.09	0.33 ± 0.09	0.47 ± 0.26	0.011 ± 0.014
ratio to O			1.00	0.20 ± 0.08	0.23 ± 0.09	0.33 ± 0.20	0.008 ± 0.010
Remnant	0.6	100	1.046 ± 0.250	0.243 ± 0.059	0.221 ± 0.061	0.268±0.143	0.033 ± 0.009
Near-side ejecta	0.6	(170)[a]	1.57 ± 0.44	0.35 ± 0.10	0.35 ± 0.10	0.42 ± 0.24	0.024 ± 0.018
ratio to O			1.00	0.19 ± 0.08	0.27 ± 0.11	0.46 ± 0.28	0.003 ± 0.015
remnant	2.4	100	0.490 ± 0.106	0.103 ± 0.023	0.111 ± 0.028	0.188±0.091	0.020 ± 0.005
Far-side ejecta	2.4	(384)[a]	1.40 ± 0.47	0.26 ± 0.011	0.38 ± 0.11	0.64 ± 0.35	0.004 ± 0.038
ratio to O			1.00	0.19 ± 0.08	0.27 ± 0.11	0.46 ± 0.28	0.003 ± 0.015

Note.
[a] Numbers in parentheses refer to mixture of ISM and ejecta.

Although there is appreciable scatter in the individual calculations, there are general trends in these published results. The most abundant element in the debris is always O. Below a precursor mass of 30 $M_\odot$, the more massive the star, the greater the yield of O; it takes an ≈20 $M_\odot$ star to produce 1 $M_\odot$ of O. The mass of Ne in the ejecta is ∼0.1–0.2 that of O and the mass of Mg is ∼0.2–0.5 that of Ne.

Table 6 compares the observation results with selected explosion calculations that are close to observed values for O and Ne. The first four models show results close to the masses actually observed. If all the debris is present in the interior hot plasma and radiating, this comparison is valid. Note that observed values are not sensitive to the ISM column used to calculate X-ray absorption (see Table 5). Observed masses of O and Ne are usually compatible with precursor star masses of 18–22 $M_\odot$, but sometimes the calculated Ne mass is low. The observed Mg mass, however, is always significantly higher than predicted. The calculated Mg/Ne ratio is usually in the range 1/4–1/3 for all the explosions, whereas the observed ratio is ≈1. Observed Si upper limits are compatible with most calculations, whereas the calculated Fe values all exceed our upper limit by 50% or more. In this group, the best fit to observation is the TNY 20 model.

The second group in Table 6 compares material from more massive precursors with the observed mass plus mass from an assumed southern extension of the northern X-ray-bright crescent. We previously speculated that all the ejecta might not be hot enough to emit X-rays. In particular, a southern arc of unseen material would make the remnant symmetrical. Also, the thermal energy inside the remnant was measured to be half that predicted by the scaled Chevalier model, which implies half the ejecta is too cool to detect. However, the addition of a southern crescent increases the ejecta masses by only ≈40%. The best fit here is TNY 25. As usual, Mg is low but the Fe mass is now below our upper limit. Other calculated 25 $M_\odot$ explosions produce too much O and too much Fe for this full-shell, increased-mass assumption. Ne masses agree with observation, predicted Mg masses are still too low, and predicted Fe masses are high.

In summary, the masses measured for these light-element ejecta are not far from those calculated for some explosions. The only real discrepancy is a factor of 3 in the mass of Mg. We note that large abundances of Mg have been noticed in other younger LMC remnants, e.g., N49B (Park et al. 2003) and N206 (Williams et al. 2005), although relative masses for those remnants were not derived. Actually, our Mg "observed mass" is probably 20% high because the central region where Mg is concentrated is at higher temperature than that determined using the spectrum of all the emitting material. Some detail is given in Sections 3.3 and 3.4.

The following remnant history fits this observation. At an age of ∼40 kyr the adiabatically expanding remnant was symmetrical with X-ray emission filling the interior. At this time the expanding shell started to cool and to collide with the nearby northern Hα filament, a fairly substantial structure probably held together by a magnetic field. This collision is still ongoing, and some of the filament is now pushed to the north ahead of the expanding dense shell of the remnant. A shock has propagated south, heating material in the interior and in the dense shell, which now has optically bright sections at the location of the collision. The interior material, at age ∼100 kyr without the collision, would have been too cool to emit X-rays, but the northern half has been reheated by the collision shock and forms the observed X-ray crescent. This also explains the unusual radio feature—also a crescent but interior to the forward shock and predominately on the north side of the remnant. The collision shock has accelerated electrons and perhaps compressed the magnetic field in this region to the point where radio synchrotron emission occurs. Bozzetto et al. (2012) measure radio polarization and comment that it and the radio spectrum are more characteristic of younger remnants than one this old. This fits the collision-shock hypothesis. O and Ne masses in the ejecta indicate that the progenitor mass was ≈20 $M_\odot$ and maybe a bit higher due to unseen material in the south. An even more massive progenitor is not impossible.

6. Serendipitous Sources and the Search for a Neutron Star

Since this remnant is probably the result of core collapse, we searched for a NS formed by that collapse. At birth, or at least early in life, NSs are generally propelled away from the site of the explosion, with typical velocities of several hundred kilometers per second (Verbunt et al. 2017). Some have velocities of 1000 km s^{-1} or more (Cordes et al. 1993; Pavan et al. 2011), and with these velocities can travel 1 pc in 1 kyr, or ≈100 pc in the age of this remnant and, if transverse, ≈7′ in the LMC. We looked at serendipitous sources within a distance of 5′ from the center of the remnant ($05^h50^m28^s.6$, $-68°23'37''$),

Table 6
Comparison with Nucleosynthesis Calculations for Type II SNe

	Measured ($M_\odot$)	Reference					Full Shell ($M_\odot$)	Reference			
		WW S18	WW S19	WW S20	TNY 20	WW T20		WW S22	WW S25	TNY 25	SEW 25
O	1.41 ± 0.36	1.13	1.43	1.94	1.48	1.62	2.03 ± 0.50	2.38	3.25	2.99	3.57
Ne	0.28 ± 0.09	0.29	0.12	0.13	0.26	0.055	0.42 ± 0.14	0.11	0.44	0.63	0.36
Mg	0.33 ± 0.09	0.077	0.046	0.049	0.18	0.017	0.50 ± 0.13	0.062	0.16	0.23	0.11
Si	<0.73	0.15	0.28	0.30	0.10	0.24	⋯	0.25	0.34	0.38	0.44
Fe	<0.05	0.092	0.13	0.12	0.078	0.073	<0.07	0.24	0.17	0.058	0.15

Table 7
Counterparts of Nearby Serendipitous X-Ray Sources

No.	Sep. (arcsec)	Position (2000) (R.A., decl.)	Rrr Rad. (arcsec)	Sig.	ACIS (cnts)	Spitzer SAGE Sep. 3.5 μm/4.5 μm (arcsec)	Gaia Sep. G/BP mag (arcsec)	2MASS Sep. J mag (arcsec)	Class.
1	103	$05^{h}50^{m}47^{s}49$–68°23′35″32	1.04/0.79	3.14	17	0.24 14.4/14.4	0.39 18.4/19.0	0.42 15.6	Star
2	119	$05^{h}50^{m}47^{s}46$–68°24′36″85	1.12/0.8	5.8	46	⋯	2.2 20.5/21.1	⋯	No ctp.
3	125	$05^{h}50^{m}13^{s}22$–68°25′09″14	2.41/1.33	2.83	17	⋯	2.1 20.5/20.2	⋯	Star
4	140	$05^{h}50^{m}38^{s}60$–68°21′27″52	0.76/0.74	4.71	27	⋯	⋯	⋯	No ctp.
5	142	$05^{h}50^{m}11^{s}46$–68°25′22″58	0.91/0.78	10.8	135	0.55 16.7/15.7	⋯	⋯	AGN
6	143	$05^{h}50^{m}50^{s}02$–68°22′14″89	0.84/0.75	3.53	13	⋯	⋯	⋯	No ctp.
7	149	$05^{h}50^{m}41^{s}91$–68°21′26″50	0.74/0.74	4.06	20	0.07 16.5/16.0	⋯	⋯	AGN
8	163	$05^{h}50^{m}29^{s}75$–68°20′54″08	0.78/0.77	3.17	14	⋯	⋯	⋯	No ctp.
9	163	$05^{h}50^{m}32^{s}32$–68°20′54″72	0.72/0.72	10.1	135	0.11 17.4/16.9	⋯	⋯	AGN
10	171	$05^{h}50^{m}55^{s}90$–68°25′00″69	1.53/1.23	3.2	11	0.15 12.8/12.8	0.22 14.0/14.3	0.20 13.1	Star
11	183	$05^{h}50^{m}02^{s}94$–68°21′40″81	1.15/0.86	3.11	13	0.61 15.7/15.7	0.70 15.9 19.9	0.53 16.7	Star
12	193	$05^{h}50^{m}54^{s}69$–68°21′27″88	0.76/0.73	4.37	24	0.27 16.2/16.1	⋯	⋯	AGN
13	195	$05^{h}50^{m}42^{s}37$–68°20′36″41	0.74/0.73	3.29	12	0.34 17.3/16.6	⋯	⋯	AGN
14	201	$05^{h}50^{m}12^{s}23$–68°26′37″11	1.88/1.88	3.24	13	3.10 16.2/16.0	3.2 19.9/20.8	⋯	Star?
15	210	$05^{h}50^{m}50^{s}.58$–68°26′29″48	1.42/0.94	7.94	92	0.20 16.5/16.2	⋯	⋯	AGN
16	221	$05^{h}50^{m}58^{s}34$–68°21′08″52	0.79/0.75	3.59	16	0.05 17.7/17.2	⋯	⋯	AGN
17	241	05^{h} 51^{m} $10^{s}49$–68°22′27″17	1.27/0.93	2.83	12	0.35 17.4/17.2	⋯	⋯	AGN
18	248	05^{h} 51^{m} $05^{s}89$–68°21′18″39	1.08/0.81	3.76	17	⋯	⋯	⋯	No ctp.
19	268	$05^{h}50^{m}56^{s}44$–68°19′56″94	0.76/0.75	3.64	17	0.12 17.2/16.6	⋯	⋯	AGN
20	271	05^{h} 49^{m} $56^{s}74$–68°20′11″48	0.77/0.74	7.87	82	0.22 17.7/16.9	⋯	⋯	AGN
21	271	05^{h} 49^{m} $55^{s}65$–68°20′16″09	0.84/0.76	9.11	106	⋯	1.29 19.0/19.5	1.33 17.4	Star?
22	286	$05^{h}50^{m}54^{s}10$–68°19′27″73	0.83/0.79	2.81	11	1.10 17.6/17.1	⋯	⋯	AGN
23	286	$05^{h}50^{m}27^{s}23$–68°18′50″15	0.76/0.74	4.37	28	0.10 16.4/16.0	⋯	⋯	AGN
24	312	$05^{h}49^{m}53^{s}0$–68°19′44″	1/1?	na	600	0.12 10.5/10.6	0.24 13.6	0.25 11.5	Star?

which includes all but the corners of the 8′ square ACIS chip field and will include any NS with velocity $\leqslant$600 km s^{-1}.

The Chandra Source Catalog (CSC; Evans et al. 2010, Primini et al. 2011) lists 32 serendipitous point sources in this 5′ radius field. The 23 brightest are listed in Table 7 and their hardness ratios are shown in Figure 7. Information in columns 2–5 of Table 7 is from the CSC and lists coordinates and location accuracies for the sources plotted in Figure 7. We searched for counterparts at the same locations using VizieR.[5] We used the 3–8 μm Spitzer SAGE survey[6] for IR sources and the 0.5–0.9 μm Gaia catalog[7] for stars. We expected most serendipitous sources to be background active galactic nuclei (AGNs), and, indeed, 16 out of 23 objects have SAGE counterparts. Some SAGE locations overlap the six Gaia counterparts found.

In Table 7, column 2 gives the distance from the remnant center, column 3 the X-ray source coordinates (epoch 2000), column 4 the semimajor and semiminor axes of the Chandra 95% confidence level error ellipse, and column 5 the significance of the source (estimate of ratio of flux to its average error). Column 6 gives the number of counts above background in the ACIS data. Columns 7 and 8 concern the search for counterparts, and give the separation of X-ray and counterpart locations and the brightness of the nearest Spitzer SAGE and/or Gaia objects. Column 9 adds 2MASS J magnitudes for some of the Gaia objects. A separation of more than 1.5× the Chandra error radius was considered an accidental overlap. The locations of sources 14, and 21 are close to this critical distance from the potential counterpart and the "?" in the last column reflects this uncertainty in the given classification. Chandra sources with no SAGE or Gaia coounterparts are classified "no ctp.". Note that the AGN classification here is based solely on the positive detection by Spitzer, except for the radio-bright source 9, which is the only known AGN in our list. The probability of accidental overlap depends on the density of SAGE or Gaia objects in the field. These catalogs have 21 and 45 sources arcmin^{-2}, respectively, with a location accuracy of 0.″3 and <0.″01. So, for a Chandra

[5] http://vizier.u-strasbg.fr/viz-bin/VizieR-2
[6] II305/catalog.
[7] I350/gaiadr3.

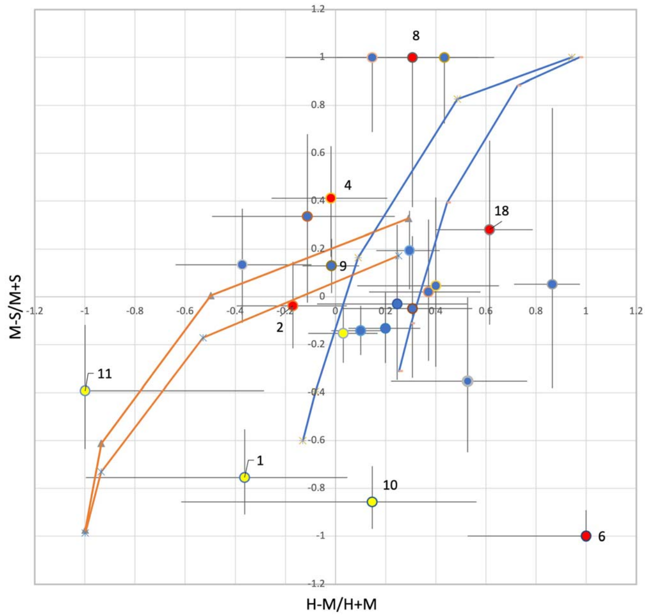

Figure 7. A color–color plot of hardness ratios for the sources listed in Table 7. See text for data point details. The two blue lines show locii for power-law spectra and the two orange lines blackbody. Soft sources will appear at lower left and hard or strongly absorbed sources at upper right.

location with 1″ error radius, the probabilities of accidental SAGE or Gaia counterparts are 2% and 4%.

Most of the serendipitous sources should be AGNs; in this observation, ∼30 are expected (Brandt & Hasinger 2005). Most are visible at near/mid-IR wavelengths in the Spitzer SAGE survey (Meixner et al. 2006). In the X-ray band these should show as point sources with power-law spectra, but there are usually too few counts to to get an accurate spectrum. However, some information for these sources is available from the CSC, which lists photon fluxes at the telescope aperture in three energy bands: H (2–7 keV), M (1.2–2 keV), and S (0.5–1.2 keV) These are used for each source to generate two hardness ratios, $(H-M)/(H+M)$ and $(M-S)/(M+S)$, which are plotted in Figure 7. In this figure the expectations for power-law spectra are shown by two blue curves. The upper blue curve is for a photon index of −2.5 and the lower for an index of −1.5. AGN spectra should generally fall between these two curves (Wilkes & Elvis 1987). Inflection points occur at absorptions of (0.1, 0.3, 1, 3, 10) $\times 10^{22}$ atoms cm^{-2}. Of course, power-law spectra alone cannot be used to distinguish between a young energetic NS with pulsar wind nebula and an AGN, and we do not attempt to do so here. An older NS, however, will radiate like a blackbody, as has been observed (Haberl 2007). In Figure 7 blackbody spectra hardness ratios are indicated by the two orange curves. The upper orange curve is for an interstellar absorption column of 1×10^{21} atoms cm^{-2}, the lower for a thickness of 3×10^{21}, bracketing the range expected for objects in the LMC at this location. Blackbody temperature ranges from 0.1 keV at lower left to 0.8 keV at upper right.

Hardness ratios can distinguish spectra for the brighter sources, but for the fainter the error bars are too large for the ratio to be useful and so only the brighter 23 sources listed by the CSC are plotted here. Source 24 in Table 7 is not in the CSC because it is exactly on the edge of the ACIS chip. Since it is the brightest point source in the field, it is included here (with a less accurate location) for completeness.

Table 8
X-Ray Spectrum of AGN J055032.5-682054

N_H (absorption, 10^{22} atoms cm^{-2})	0.45 ± 0.27
Power-law photon index, 0.3–4 keV	-2.3 ± 0.8
Absorbed flux, 0.3–8 keV (erg cm^{-2} s^{-1})	1.5×10^{-14}
Unabsorbed flux 0.3–8 keV (erg cm^{-2} s^{-1})	3.5×10^{-14}

Table 9
Broadband Spectrum

λ or $h\nu$	ν (s^{-1})	Flux Density (Jy)	Flux (s^{-1} Jy)
36 cm	8.3×10^{8}	1.32×10^{-1}	1.1×10^{8}
20 cm	1.5×10^{9}	8.6×10^{-2}	1.3×10^{8}
6 cm	5×10^{9}	2.4×10^{-2}	1.2×10^{8}
3 cm	1×10^{10}	7×10^{-3}	7×10^{7}
4.5 μm	6.67×10^{13}	2.7×10^{-5}	1.8×10^{9}
3.5 μm	8.57×10^{13}	3.1×10^{-5}	2.7×10^{9}
0.5 keV	1.2×10^{17}	11.8×10^{-9}	1.4×10^{9}
2.0 keV	4.8×10^{17}	1.87×10^{-9}	0.9×10^{9}

We are searching for an isolated NS in the LMC, not so bright for it to be immediately obvious, but bright enough to hint at its character. At this distance, it would have no detectable counterpart at IR or optical wavelengths. Sources 2, 4, 6, 8, and 18 have no counterparts in the catalogs searched. Note that sources 1, 6, 10, and 11 form a group spread at the bottom of Figure 7. Since 1, 10, and 11 are all associated with bright Two Micron All Sky Survey (2MASS) stars, source 6 is probably a fainter star of this type. The ratios of sources 2, 4, 8, and 18 are all compatible with an AGN origin. Source 2 also fits the expectation for a blackbody spectrum and is probably the best candidates for a NS. Source 2 can be seen in Figure 3 and is actually inside the remnant close to the southwest boundary. A deep optical observation is necessary to carry this search further. Of course, a NS with the age of the remnant is expected to have faded to an X-ray luminosity below our detection threshold of $\approx 10^{32}$ erg s^{-1}, but a more luminous object than expected is always possible.

7. The Radio-bright AGN J055032.5-682054

This point-like radio source, so close to the remnant, was originally thought to be associated with it, thus making an X-ray observation worthwhile. Here are the AGN results as a matter of general interest. In this observation, 135 X-ray counts were obtained, enough for a simple power-law spectral fit, and the best-fit parameters are given in Table 8. To investigate the broadband properties, we used radio fluxes summarized by Bozzetto et al. (2012) and the two IR magnitudes listed in Table 7. The broadband spectrum can be compared with that of other radio-loud and radio-quiet AGNs, as reviewed by Elvis et al. (1994), making use of $E^2 \times dN/dE$, $\nu f(\nu)$ plots. Table 9 lists information for this AGN.

The value of $\nu(f\nu)$ for both X-rays and IR is $\approx 10^{8}$ s^{-1} Jy (10^{-18} W m^{-2}). Apparently, this approximate agreement is normal for most AGNs. However, the radio flux for our AGN is only a factor of 10 below that of the X-rays, in contrast to the factor of 10^{4} below characteristic of radio-quiet AGNs. So this object is radio-loud. Compared with other radio-loud AGNs the X-ray spectrum is unusually soft (Wilkes & Elvis 1987).

Acknowledgments

We acknowledge many enlightening discussions with colleagues at CfA, particularly Martin Elvis, Mike McCollough, Frank Primini, and Randall Smith. Bill Joye and Kyle Welch helped with computer problems. F.D.S. thanks the Center for Astrophysics | Harvard & Smithsonian for support. We thank the anonymous referee for carefully reading the paper and recommending a reorganization of the presentation and more detail and references for several technical points. We acknowledge the efforts of many people who make astronomy data publicly available, formatted to be understandable and, very importantly, usable. This research has made use of data obtained from the Chandra Data Archive and from the Chandra Source Catalog. Software provided by the Chandra X-ray Center (CXC) was used for analysis. The Australian 33 cm radio survey image was obtained from CASDA, The Commonwealth Science ASKAP Science Data Archive. Optical images are from the MCELS LMC survey. The Vizier presentation of the Spitzer SAGE results and Gaia star positions made possible a search for counterparts of serendipitous X-ray sources.

ORCID iDs

Frederick D. Seward https://orcid.org/0000-0003-4232-2211
Sean D. Points https://orcid.org/0000-0002-4596-1337

References

Anders, E., & Grevesse, N. 1989, GeCoA, 53, 197
Bozzetto, L. M., Filipovic, M. D., Crawford, E. J., et al. 2012, RMxAA, 48, 41
Bozzetto, L. M., Filipovic, M. D., Sano, H., et al. 2022, MNRAS, 518, 2574
Brandt, W. N., & Hasinger, G. 2005, ARA&A, 43, 827
Chevalier, R. A. 1974, ApJ, 188, 501
Cordes, J. M., Romani, R. W., & Lundgren , S. C. 1993, Natur, 362, 133
Dickel, J. R., McIntyre, V. J., Gruendl, R. A., & Milne, D. K. 2005, AJ, 129, 790
Elvis, M., Wilkes, B. J., McDowell, J., et al. 1994, ApJS, 95, 1
Dopita, M. A. 1982, in ASI Proc. 90, Supernovae: A Survey of Current Research, ed. M.J. Rees & R.J. Stoneham (Dordrecht: Springer), 483
Evans, I. N., Primini, F. A., Glotfelty, K. J., et al. 2010, ApJS, 189, 37
Freeman, P., Doe, S., & Siemiginowska, A. 2001, Proc. SPIE, 4477, 76
Güver, T., & Özel, F. 2009, Ap&SS, 324, 17
Haberl, F. 2007, Ap&SS, 308, 181
Long, K. S., Blair, W. P., Winkler, P. F., et al. 2010, ApJS, 187, 495
Maggi, P., Haberl, F., Kavanagh, P. J., et al. 2016, A&A, 585, 162
Meixner, M., Gordon, K. D., Indebetouw, R., et al. 2006, AJ, 132, 2268
Morrison, R., & McCammon, D. 1983, ApJ, 270, 119
Park, S., Hughes, J., & Slane, P. 2003, ApJ, 592, 41
Pavan, L., Bozzo, E., Puhlhofer, G., et al. 2011, A&A, 533, A74
Pennock, C. M., van Loon, J. T., Filipovic, M. D., et al. 2021, MNRAS, 506, 3540
Primini, F. A., Houck, J., Davis, J., et al. 2011, ApJS, 194, 37
Rozas, M., Richer, M. G., Lopez, J. A., et al. 2006, A&A, 455, 539
Sasaki, M., Pietsch, W., Haberl, F., et al. 2012, A&A, 544, A144
Schenck, A., Park, S., & Post, S. 2016, AJ, 151, 161
Seward, F. D., Foster, A. R., Smith, R. K., & Points, S. D. 2021, ApJ, 909, 13
Seward, F. D., Smith, R. K., Slane, P. O., et al. 2018, ApJ, 861, 154
Smith, R. C. & MCELS Team 1998, PASA, 15, 163
Staveley-Smith, L., Kim, S., Calabretta, M. R., et al. 2003, MNRAS, 339, 87
Sukhbold, T., Eril, T., Woosley, S. E., Brown, J. M., & Janka, H.-T. 2016, ApJ, 821, 38
Tsujimoto, T., Nomoto, K., Yoshii, Y., et al. 1995, MNRAS, 277, 945
Verbunt, F., Igoshev, A., & Cator, E. 2017, A&A, 608, A57
Wilkes, B. J., & Elvis, M. 1987, ApJ, 323, 243
Williams, R. M., Chu, Y. H., Dickel, J. R., et al. 2005, ApJ, 628, 704
Woosley, S. E., & Weaver, T. A. 1995, ApJS, 101, 181
Zaritsky, D., Harris, J., Thompson, I. B., & Grebel, E. K. 2004, AJ, 128, 1606